Deep–Sea Research I 206 (2024) 104277

Contents lists available at ScienceDirect

Deep-Sea Research Part I

journal homepage: www.elsevier.com/locate/dsri

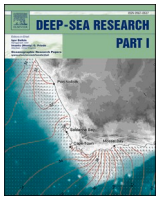

Near-slope turbulence in a Rockall canyon

Hans van Haren [a,*], Gunnar Voet [b], Matthew H. Alford [b], Bieito Fernández-Castro [c], Alberto C. Naveira Garabato [c], Bethan L. Wynne-Cattanach [b], Herlé Mercier [d], Marie-José Messias [e]

[a] Royal Netherlands Institute for Sea Research (NIOZ), P.O. Box 59, 1790 AB, Den Burg, the Netherlands
[b] Scripps Institution of Oceanography, UC San Diego, Mail Code 0213, La Jolla, CA, 92093-0213, USA
[c] Ocean and Earth Science, University of Southampton, Southampton, SO14 3ZH, UK
[d] University of Brest, CNRS, Ifremer, IRD, Laboratoire d'Océanographie Physique et Spatiale (LOPS), IUEM, Plouzané, 29280, France
[e] University of Exeter, Streatham Campus, Laver Building, North Park Road, Exeter, Devon, EX4 4QE, UK

ARTICLE INFO

Keywords:
Steep rockall canyon slope
103 high-resolution temperature sensors
moored between [0.9 152]m
Turbulence values increase towards seafloor
Dominant convection in lower 5 m

ABSTRACT

The acknowledgement of the importance of small-scale turbulent mixing for the redistribution of heat, nutrients and suspended matter in the ocean has led to renewed interest in the breaking of internal waves at underwater topography. This follows from observations that turbulence intensity increases from the ocean interior to the seafloor. As two-dimensional models require reduction of turbulent buoyancy flux in the vicinity of the seafloor to allow for up-welling flows, the question is how thin such a layer of reduced turbulence above the seafloor can be. From an observational study in this subject, we present 400-day moored high-resolution temperature measurements in a Rockall canyon between $0.9 < h < 152$ m from the steeply sloping thalweg-seafloor. In the area, Thorpe-scale calculated turbulence dissipation rate is predominantly governed by the breaking of semidiurnal internal tides. Tidal-mean turbulence profiles increase with depth, together with inertial-subrange temperature-variance. A distinct further increase in turbulence is found for the lower 4 m across which inertial-subrange temperature variance decreased. This was observed during most of a tidal phase, except during the warming phase, when a decrease in turbulence was found in the lower few meters. The thin layer above the seafloor showed a distinct change in distribution of small-scale stratification and a transition from little inertial-subrange variance at $h = 0.9$ m, via dominant convection-turbulence at $h < 5$ m to dominant shear-turbulence at $h > 30$ m, as established from spectral information. The lack of an observed mean near-seafloor buoyancy-flux reduction is hypothesized to be compensated by 3D-effects, temporary effects, less steep slope effects, or none at all.

1. Introduction

The conjecture that the ocean remains vertically stably stratified via sufficient "small-scale" turbulent mixing has led to the suggestion that most mixing occurs near the seafloor, which is generally not flat (e.g., Armi, 1978; Armi, 1979). Although considerable work has been performed on understanding the mixing via frictional flows in a 'boundary layer' above sloping topography (e.g., Weatherly and Martin, 1978; Garrett, 1990; MacCready and Rhines, 1991; Brink and Lentz, 2010), most turbulent mixing near sloping topography seems to be invoked by breaking internal waves (Wunsch, 1970; Eriksen, 1982; Thorpe, 1987; van Haren et al., 1994; Sarkar and Scotti, 2017). The difference in mechanism of turbulence generation may be fundamental for the resulting mean flow.

While an advection-diffusion balance of steadily reducing turbulent mixing as a function of distance from the ocean surface leading to up-welling flows in the interior has been proposed (Munk, 1966; Munk and Wunsch, 1998), the observational evidence of turbulent mixing increasing from the interior to the notably sloping seafloor leading to down-welling interior flows has led to the suggestion of up-welling in a thin layer above the seafloor (de Lavergne et al., 2016; Ferrari et al., 2016; McDougall and Ferrari, 2017). The conjecture in these latter studies is that the turbulence must be reduced at the seafloor, following the Prandtl concept of a frictional boundary layer of well-mixed waters (Anderson, 2005).

The above conjectures lead to the following questions. How thin can such a layer of up-welling flow be above the seafloor? As the Prandtl concept has been devised for a two-dimensional (2D) plate, is it valid in a 3D region of highly variable seafloor topography and turbulence primarily induced by breaking internal waves? Are there regions that favor

* Corresponding author.
E-mail address: hans.van.haren@nioz.nl (H. van Haren).

https://doi.org/10.1016/j.dsr.2024.104277
Received 3 October 2023; Received in revised form 1 February 2024; Accepted 28 February 2024
Available online 29 February 2024

up-welling flows more than others? For example, St. Laurent et al. (2001), Thurnherr et al. (2020) and Drake et al. (2022) consider and show up-welling mean flows along the thalweg of deep-ocean canyons and fracture zones, but down-welling flows otherwise.

Observational evidence shows ambiguous results about the thickness of a 'boundary layer' above sloping topography. As the ocean-interior stratification supports omnipresent internal waves, their breaking above sloping topography result in highly variable turbulent mixing and restratification near the seafloor. Internal wave breaking provides a very thin layer of well-mixed waters of probably less than 3 m (van Haren et al., 1994), as established from shipborne microstructure profiler data, and which is thinner than expected for the Ekman layer O(10) m thickness of frictional steady or oscillatory flows over a flat or sloping seafloor on a rotating Earth (e.g., Weatherly and Martin, 1978; Brink and Lentz, 2010). Modelling results (Flores and Riley, 2011; Ruan et al., 2019) indicate that the reduction of stratified turbulence, induced by processes other than frictional flows, occurs within the log-layer $L < 100\nu/u_* \ll 1$ m from a (sloping) seafloor. Here, $\nu = 10^{-6}$ m^2 s^{-1} is the kinematic viscosity and friction velocity $u_* = (C_d U^2)^{0.5}$ for large-scale flow U and drag coefficient $C_d = 2.5 \times 10^{-3}$.

The very thin layer of turbulence reduction leads to the importance of restratification during a different wave phase following internal wave breaking close (<1 m) to a sloping seafloor, see e.g., modelling results by Winters (2015). In ocean observations, continuous increase of turbulent diffusivity K_z has been found down to the lowest observational level during the passage of an upslope propagating frontal bore, as opposed to a reduction of K_z during the warming phase of the tide when wave breaking does not reach the seafloor, as established using the sorting of moored high-resolution temperature-sensor observations (van Haren and Gostiaux, 2012). Internal wave breaking not only generates shear-induced turbulence but also convection-turbulence reaching close to the seafloor (van Haren, 2015).

In this paper we present results between 0.9 and about 152 m above a sloping seafloor from high-resolution temperature sensors and a low-resolution current profiler that were mounted on a very slim mooring, rather than a bulky bottom-lander frame (van Haren and Gostiaux, 2012). The mooring was in the thalweg of a canyon in the Rockall Channel, as opposed to more open topography like Great Meteor Seamount as in van Haren and Gostiaux (2012) and an East-Pacific slope (van Haren et al., 2022b). While it is noted that canyons display a complex 3D flow structure (e.g., Hall and Carter, 2011; Vlasenko et al., 2016), their importance has been suggested for intensification of internal tides (van Haren et al., 2022a) and potential for up-welling flow (St. Laurent et al., 2001; Thurnherr et al., 2020) near the thalweg seafloor. The Rockall Channel is an important throughflow, with relatively strong (internal) tides and northward boundary flow including (sub-)mesoscale meanders and eddies along its eastern slope (New and Smythe-Wright, 2001; Ullgren and White, 2012).

The objectives are the yearlong monitoring of temperature variations in the lower 150 m above the seafloor, calculating turbulence values using the method of sorting the high-resolution temperature data down to 1 m from the seafloor, and establishment of dominance of shear- or convection-induced turbulence via spectral information.

The paper is organized as follows. Section 2 gives the technical details of site, instrumentation, and post-processing. In Section 3 the observations are presented in various sub-sections. Section 4 presents the general discussion of results.

2. Technical details

2.1. Study area

Together with several other moorings to study turbulence dynamics above sloping topography, a 170-m tall taut-wire mooring 'TCHAIN' was located at 54° 11.413′N, 011° 51.137′W, H = 1525 m water depth approximately in the thalweg of a canyon in the continental (southern) slope of the Rockall Channel, NE-Atlantic Ocean (Fig. 1). The mooring was underwater for 401 days between 6 July (yearday 186) 2021 and August 10, 2022. The average local bottom slope equals about $\gamma = 0.08 = 4.5°$ computed over 1 km horizontal scales. The average angle of semidiurnal internal tide rays under local vertical density stratification conditions amounts $\beta = \beta_{M2} = \sin^{-1}((\omega^2_{M2}\text{-}f^2)^{1/2}/(N^2\text{-}f^2)^{1/2}) = 2.2° \approx \gamma/2$, using the formulation for freely propagating linear internal waves in, e.g., LeBlond and Mysak (1978). Here, lunar frequency $\omega_{M2} = 1.405 \times 10^{-4}$ s^{-1}, $f = 1.183 \times 10^{-4}$ s^{-1} the local planetary inertial frequency (Coriolis parameter), and $N = 2 \times 10^{-3}$ s^{-1} the 100-m large-scale mean local buoyancy frequency over the range of TCHAIN-mooring.

2.2. Mooring details

A single large spherical buoy holding a current profiler was at about z = −1370 m. A total of 103 'NIOZ4' high-resolution T-sensors were taped to the nylon-coated 150-m long 0.005-m diameter steel cable.

To sample temperature to within 1 m from the seafloor, two acoustic releases were placed directly at the two-train-wheel anchor-weight and connected via a 0.4 m short anchor chain between the release-links in a custom-designed construction (van Haren et al., 2022b). The impact of the free-falling mooring was minimal, a few centimeters, on the chain and cable. Thus, the custom-made set-up allowed for placement of sensors close to the seafloor on a slim taut-wire mooring not requiring a bulky bottom-lander frame. The lower 2 T-sensors were at 0.5 m intervals of which the lowest at approximately 0.9 m from the seafloor, the following 51 sensors were at 1.0 m intervals and the remaining 50 sensors were at 2.0 m intervals.

The 1.25 m diameter syntactic-foam buoy provided 2.3-kN net buoyancy to the entire assembly. Under maximum 0.5 m s^{-1} current amplitudes, the low-drag mooring did not deflect from the vertical by more than 3°, i.e., the top-buoy moved <8 m horizontally and <0.2 m vertically, as inferred from the current profilers' tilt and pressure sensors.

The top-buoy's 'downward-looking' Teledyne/RDI 75-kHz acoustic Doppler current profiler (ADCP) has four beams that are slanted at an angle of 20° to the vertical. The ADCP measured currents in three directions, **U** = [u, v, w] averaged over all beams, and acoustic echo intensity in each beam, at 9 vertical bins of 16 m. The first bin was about 20 m below the uppermost T-sensor. Bin 8 at z = −1504 m was the lowest in which good data were found not contaminated by side-lobe reflection off the seafloor. There, the beam spread or horizontal averaging distance for current components was about 100 m. The ADCP sampled 22 pings every 3 s in bursts every 14 min. Here, the data are averaged in 900 s ensemble intervals.

2.3. High-resolution temperature sensors

NIOZ4 are self-contained T-sensors, with a sensor tip smaller than 1 mm, a response time of <0.5 s, an initial drift of about 1×10^{-3} °C mo^{-1} after aging of the thermistor-electronics, a noise level of $<1 \times 10^{-4}$ °C, a precision (relative accuracy) better than 5×10^{-4} °C after drift-correction for standard programmed measuring of the Wien Bridge oscillator for the duration of 0.12 s per sample (van Haren, 2018). The T-sensors sampled at a rate of 0.5 Hz. Every 4 h, all sensors are synchronized via induction to a single standard clock, so that the entire 152-m vertical range is sampled in less than 0.02 s. Of the 103 T-sensors, 4 showed calibration, noise, battery, or other electronic problems after 200 days underwater, and 1 was mechanically shifted along the cable upon recovery. The data of these sensors are replaced by linear interpolation between neighboring sensors. Due to unknown reasons more than half of the T-sensors in this mooring set-up showed negative 0.005°C-spikes at 5–30 s intervals in the data records. Although these spikes barely affect the turbulence values studied here, they are effectively removed using a low-pass filter (lpf) with a cut-off at 3000 cpd (short for cycles per day).

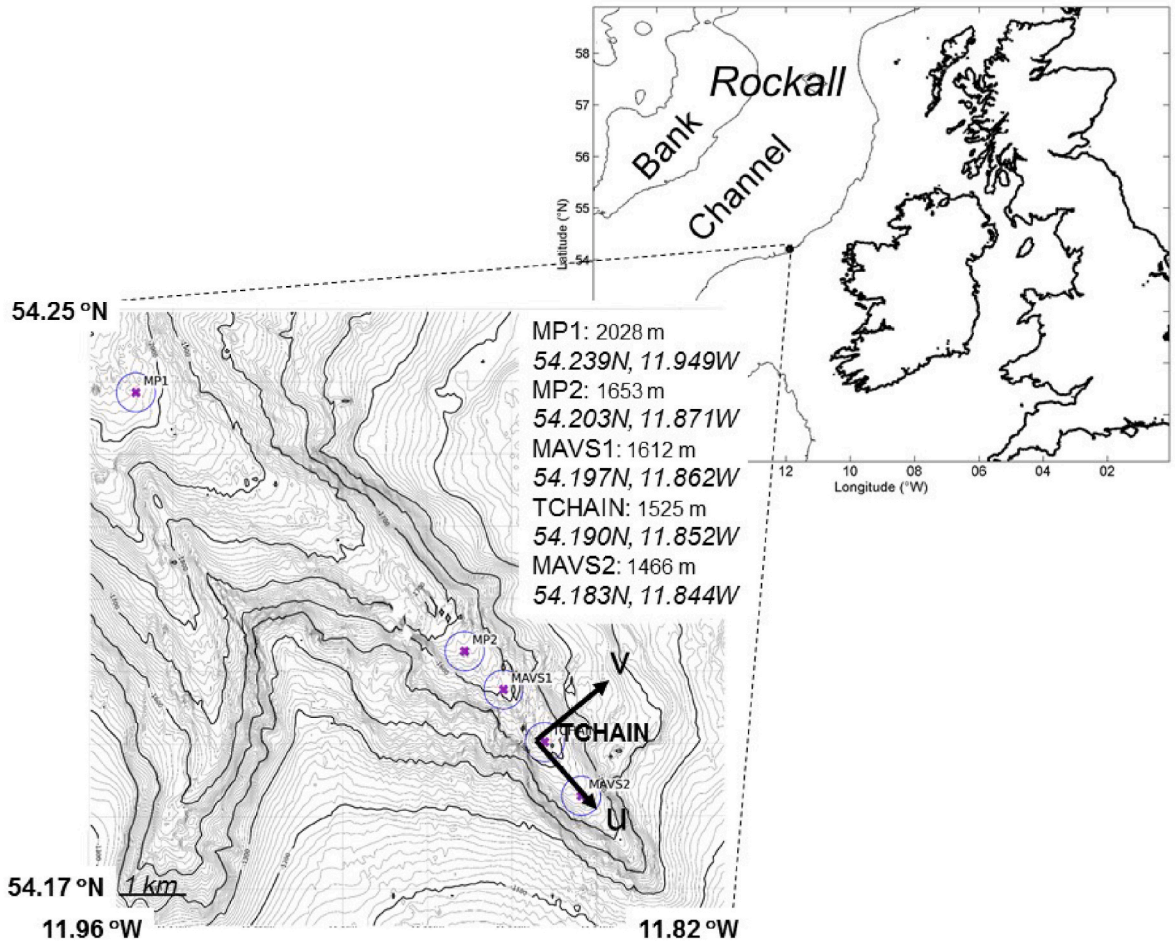

Fig. 1. Mooring site (black dot) in a canyon of the southern, continental, seafloor slope of the Rockall Channel, NE-Atlantic Ocean, together with local along-canyon (u) and cross-canyon (v) current directions. The bathymetry in the overview is from 1′-version of Smith and Sandwell (1997), in the detail from Multibeam.

Temperature data are converted into 'Conservative' (~potential) Temperature data Θ (IOC, SCOR, IOC SCOR IAPSO, 2010). They act as tracer for variations in density anomaly σ_2 following the relation $\delta\sigma_2 = \alpha\delta\Theta$, $\alpha = -0.1040 \pm 0.0004$ kg m^{-3} °C^{-1} (Fig. 2), where subscript 2 indicates a pressure reference of 2000 dbar (1 dbar = 10^4 Pa). This relation is established from data between $-1570 < z < -1270$ m of a shipborne Conductivity-Temperature-Depth (CTD)-profile obtained about 1 km from the mooring site. The CTD-data are also used for referencing the moored T-sensors during drift-correction. The moored T-sensor data are used to calculate high-resolution time series of turbulence dissipation rate ε and K_z, for details see Appendix A.

3. Observations

The vertical profiles of shipborne CTD data demonstrate steady decreases of temperature, by about 3 °C, and salinity, by about 0.2 g kg^{-1}, with depth, which implies that temperature is the dominant contributor to stable vertical density variations (Fig. 2). While the profiles do show some stepping, variations in vertical gradients of density, and small inversions, the stratification is non-zero all the way to the lowest measurement at about 5 m from the seafloor. The two-day mean moored T-sensor data around the time of CTD profiling show a consistent overall temperature gradient.

An eight-day magnification from the 400-day time series of T-sensor data, obtained about 3 months after deployment, shows that the full vertical extent of the semidiurnal internal tides is not resolved by the 152-m T-sensor range (Fig. 3). The largest temperature differences occur around springtide (day 282) when relatively warm waters reach the seafloor (Fig. 3a). The observed signal mostly contains baroclinic signals, either locally or remotely generated, which dominate over other signals like local barotropic tide and sub-inertial eddies. As demonstrated previously, e.g., by van Haren and Gostiaux (2012), each individual semidiurnal period has its time-depth shape as not one of the internal tidal oscillations is the same. This reflects the well-known characteristics of nonlinear internal waves being highly intermittent, especially above sloping topography as in these observations.

Considerable turbulence extends over the entire range of observations, although variations over more than three orders of magnitude occur throughout a semidiurnal period after a reasonable amount of mixing. Turbulent overturns do not always reach to within 1 m from the seafloor, e.g., during warming tidal wave phases with $\varepsilon < 10^{-10}$ m^2 s^{-3} (Fig. 3b). While individual turbulence dissipation rate values as depicted in Fig. 3b have no quantitative meaning, as they should be averaged over their associated turbulent overturn, the image is informative for indicating sizes of overturns and their distribution in time-depth. Qualitatively, a layer of relatively large background turbulence dissipation rate is visible as a blueish band between about $z = -1475$ and -1500 (sometimes down to -1520) m during cold phases of the internal tide. This enhanced background dissipation rate is accompanied by a band of larger background buoyancy frequency, which is yellow in Fig. 3c, albeit not deeper than $z = -1500$ m. The band of elevated background stratification and dissipation rate is not related to calibration and post-processing and is hypothesized to be related with unknown side-effects of the canyon. In a thin layer just above the seafloor, stratification seems increased in comparison with higher up, during both strongly and weakly stratified phases in a semidiurnal period (Fig. 3c). In time

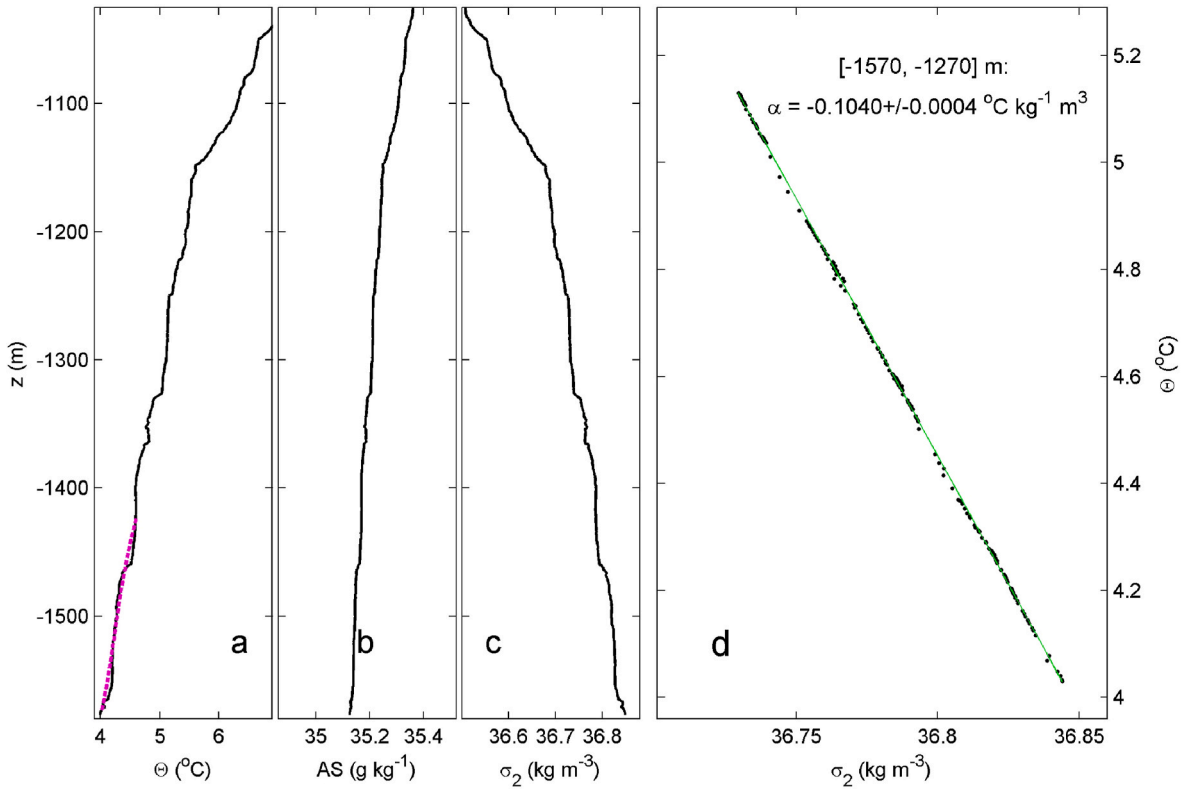

Fig. 2. Shipborne CTD-observations down to 5 m above the seafloor in the vicinity of the T-sensor mooring, obtained around the time of mooring deployment. (a) Conservative Temperature. The purple-dashed line shows the mean profile from moored T-sensor data between days 192–194, lowered by 50 m to fit the CTD-station's water depth. (b) Absolute Salinity. The x-axis range approximately corresponds with that of a. in terms of density contributions. (c) Density anomaly referenced to 2000 dbar. (d) Conservative Temperature-density anomaly relationship with linear fit in green, from the lower 300 m of the CTD-profile.

series of 152-m vertically averaged turbulence dissipation rate values which encompass most of the largest turbulent overturns reaching (close to) the seafloor, semidiurnal periodicity is well discernible, and which is overprinted with short-scale peaks that are not noise (Fig. 3d). Largest short-scale peaks occur around springtide and are part of individual >50 m tall overturns, which cannot be seen from the 152-m vertical averages but will be clearer in further magnifications presented below.

3.1. Two-day springtide detail

3.1.1. Temperature and turbulence variations

In a two-day detail around local (internal) springtide, the dominant nonlinear semidiurnal periodicity shows in temperature as well as in turbulence values (Fig. 4). While isotherms demonstrate a saw-tooth pattern of a relatively long warming phase with gradually sloping isotherms and shorter cooling phase with more vertical isotherms (Fig. 4a), the vertically averaged turbulence dissipation rate has a more symmetric shape in time but with relatively sharp peaks and troughs (Fig. 4d). Short-scale internal-wave variations are visible. In general, intense overturns seem to occur where stratification is relatively weak as was found for the upper ocean (Alford and Pinkel, 2000), compare Fig. 4b with Fig. 4c, but further magnifying focus is required for precise establishment. The very thin layer of relatively enhanced stratification near the seafloor seems to be partially associated with relatively lower dissipation rates, e.g., around days 281.2 and 282.8, contrary to expectations from equation (A.1) and thus being associated with (considerably) smaller displacements or overturns. This will be further pursued below.

The two-day spring-tide image is partially representative for the entire 400-day record, although a neap-tide image shows some characteristics (Fig. B1). While the overall mean turbulence dissipation rate during neaps is smaller but not significantly different from, that of the spring-tide period of Fig. 4, $[<\varepsilon>] = 2 \pm 1.5 \times 10^{-7}$ versus $3 \pm 2 \times 10^{-7}$ m^2 s^{-3}, the number of isotherms is reduced from 4 to 3 with cooler temperatures in Fig. B1. Diurnal inequality, modulation of the semidiurnal by diurnal motions, seems larger during neaps than during springs. In comparison with Fig. 4, non-averaged turbulence dissipation rate values seem to organize more in zones of high values (Fig. B1b), such as during the transition from warming to cooling phase and later during the cooling phase with very large overturns (Fig. B1b,c), and zones of very low values, such as notably during most of the warming phase. The vertically averaged turbulence dissipation rate values do show a semidiurnal periodicity, which is overprinted with a quasi-fourth-diurnal periodicity (Fig. B1d). Like in Fig. 4c, the small-scale buoyancy frequency in Fig. B1c seems enhanced very close to the seafloor.

3.1.2. Currents

Although the ADCP shows more than one order of magnitude coarser time-depth sampling than the T-sensors, and the upper 20 m but especially the lower 10 m of the T-sensor range are not covered by ADCP-measurements, some additional information is obtained (Fig. 5). In the two-day detail around local (internal) springtide, the dominant semidiurnal periodicity is seen in the along-canyon and vertical current components and in acoustic amplitude, while less in the cross-canyon current component.

The component with largest current amplitudes is directed along-canyon, with a weak tendency for amplitude-enhancement closer to the seafloor (Fig. 5a). This enhancement towards the seafloor is less clear than reported for Whittard Canyon (van Haren et al., 2022a). The transition from warming downslope to cooling upslope phase is characterized by strong enhancement of upslope and vertical motions, commensurate with previous findings (e.g., Hosegood et al., 2004). While these authors reported a clear association also with enhanced

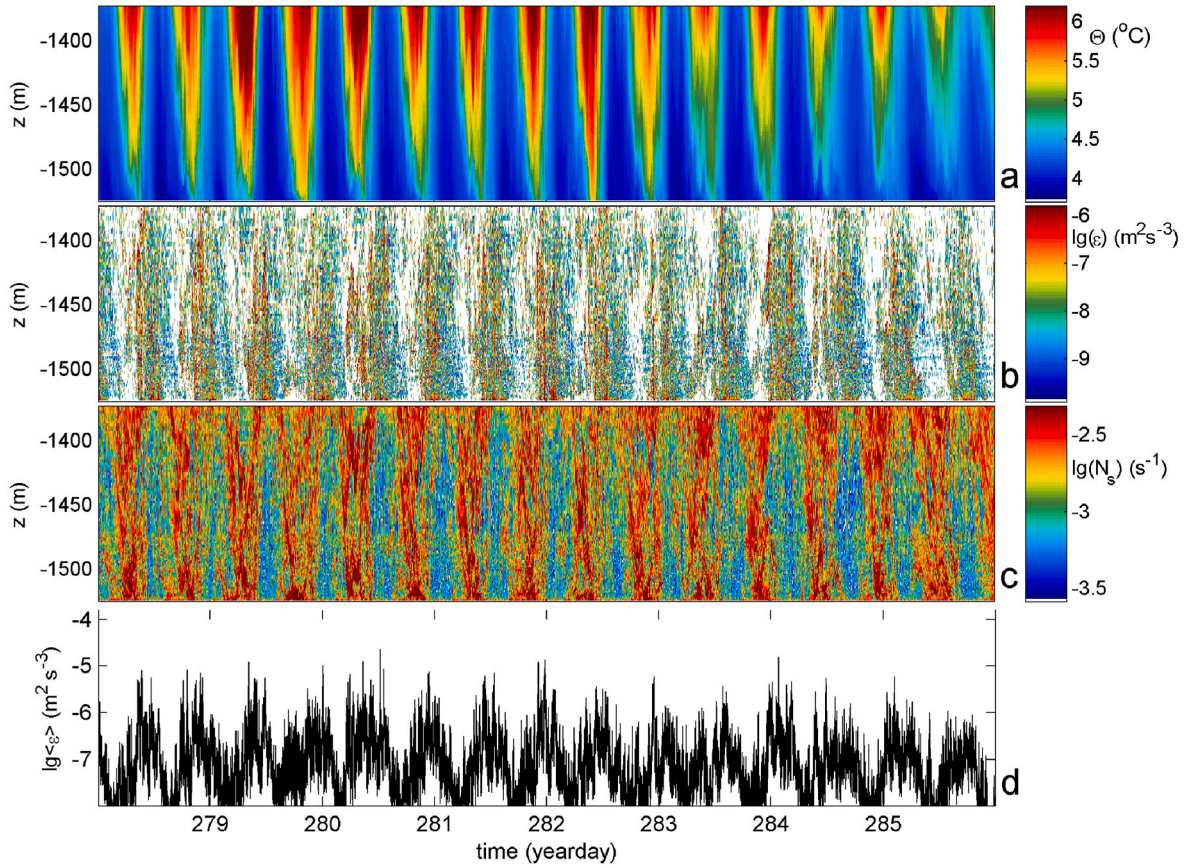

Fig. 3. Eight-day 152-m detail of moored T-sensor data sub-sampled every 20 s and calculated turbulence values. In a.-c., the horizontal axis is at the level of the seafloor. (a) Conservative Temperature. (b) Logarithm of non-averaged turbulence dissipation rate. White values are below threshold. (c) Logarithm of small-scale buoyancy frequency calculated from reordered profiles of a. (d) Logarithm of turbulence dissipation rate averaged over the vertical T-sensor range for each profile.

echo amplitude during such a passage of a frontal bore propagating over the seafloor evidencing sediment resuspension, such enhancement is not observed here (Fig. 5d). The larger relative echo amplitudes are observed at the end of the warming phase between about $-1500 < z < -1400$ m, and thus not predominantly connected with the local seafloor. This may be due to more rocky than sedimentary seafloor texture at the present site, as turbulent overturns seem to regularly reach the seafloor, also during the cooling phase (e.g., around days 281.5 and 282.0 in Fig. 4). Around these times, isotherms are near-vertical, reflecting the beginning of the cooling phase near the seafloor, and small-scale buoyancy frequencies are relatively small, with thin-layer exceptions.

3.1.3. *Buoyancy frequency distribution and definitions*

The original 2-s sampled data from the two-day detail around local (internal) springtide are taken to investigate the statistical distributions of small-scale buoyancy frequency (Fig. 6). The purpose is to learn more about the seemingly observed anomalous stratification very close to the seafloor. The probability density function (pdf) of the overall 2-d, 152-m data is close to lognormally distributed (Fig. 6a). This compares with cumulative distribution functions from observations made in the pycnocline of near-surface waters near a shelf break (Lozovatsky et al., 2021). It ranges between about $1.4 \times 10^{-4} < N_s < 1.4 \times 10^{-2}$ s^{-1}. Using the 2.5 percentiles on both sides, we arrive at definitions for minimum buoyancy frequency $N_{min} = 3.5 \times 10^{-4}$ s^{-1} (1 s^{-1} = 13751 cpd, cycles per day) and maximum buoyancy frequency $N_{max} = 5.9 \times 10^{-3}$ s^{-1}. The rms value is considered the overall large-scale mean $N = 2.4 \times 10^{-3}$ s^{-1}, which is 1.6 times the median value $N_{med} = 0.62N$. This median value is close to the frequency value associated with the top of the bulge generally found in open-ocean isotherm-displacement spectra (e.g., Munk, 1980).

From the mean buoyancy frequency and dissipation rate, a mean Ozmidov scale is computed of $L_O \approx 5$ m. This leads to a boundary-influenced regime of height $H_b = 2\pi L_O \approx 30$ m (Polzin et al., 2021; the original in Holleman et al. (2016) reads $4L_O/\kappa = 10L_O$ with κ denoting von Karman's constant) in which turbulent length scales are possibly suppressing the partitioning of turbulence production into buoyancy flux. For 1%-maximum velocity amplitude U from ADCP-measurements, the associated maximum Ozmidov frequency amounts $\omega_O = U/L_O \approx 0.07$ s^{-1}.

Throughout the vertical T-sensor range some notable deviations from the overall pdf are observed. At the lowest sensor, the distribution of lg (N_s) is approximately symmetric, but no longer Gaussian and closer to triangular, with higher values for all four buoyancy frequencies (Fig. 6b). This distribution for h = 0.9 m shows a strong deviation from lognormality, and, as will be demonstrated below, the associated temperature spectra do not show a buoyancy subrange nor an inertial subrange of turbulence. This could relate with the observed low dissipation rates. At the second T-sensor counting from the seafloor up (h = 1.4 m), the distribution is more skewed towards lower frequencies, while at T-sensors #3–6 (h = 1.9–5.4 m) counting from the seafloor up, represented by #5 (h = 4.4 m) in Fig. 6c, two relative peaks are observed in the pdf. These peaks are symmetrically distributed in lg (N_s) around the median of Fig. 6b, but the higher frequency peak shows lower counts. The extreme buoyancy frequencies N_{min} and N_{max} are virtually the same as in Fig. 6b, but the mean and median buoyancy frequencies are reduced. For sensors #7–30 (h = 6.4–29.4 m) higher up, the deviation from lognormality is a skew-shaped distribution with generally lower values for all four buoyancy frequencies (Fig. 6d) compared to those for the lower 6 T-sensors (Fig. 6b and c). This skew shape in Fig. 6d rather abruptly tends to the normally shaped distribution of Fig. 6a for T-sensor #31 and

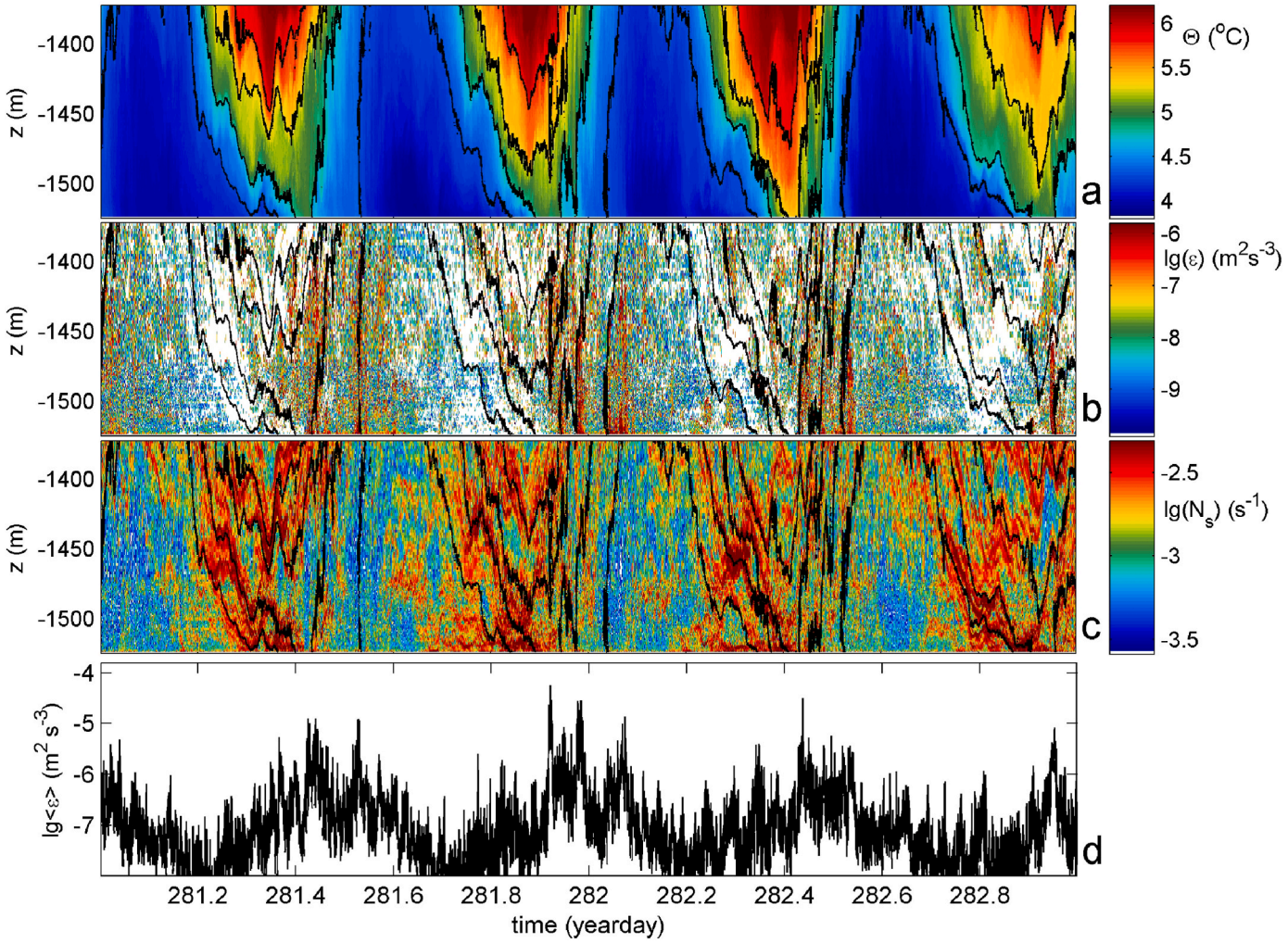

Fig. 4. As Fig. 3, but for two-day period of 4-s sub-sampled data around a spring tide. In a.-c., black isotherms are drawn every 0.5 °C.

higher (h ≥ 30.4 m). Recall that this approximately marks the band of higher background stratification values observed in Fig. 3c.

3.2. Yearlong spectra

The observed vertical variability of pdfs of lg (N_s) has some correspondence with spectral observations (Fig. 7). To further establish a dominance of shear- or convection-induced turbulence in terms of distance from the seafloor, yearlong spectra are investigated, ly in the subrange of frequencies higher than those of the internal wave band. In that subrange, spectra are compared with various spectral slopes following various (turbulence) models. Spectra are scaled with the frequency (ω) slope $\omega^{-5/3}$ of most common shear-induced inertial subrange, for clarity as the focus is on turbulence processes. Although we present 400-day long 2-s sampled data from nine selected T-sensors to provide smooth statistics, it is noted that similar results are already visible after 2 days of measurements, as has been verified by inspection of more coarsely resolved spectra for data in Fig. 4 and B1 (not shown).

The spectra are grouped in two sets of five, with the lowest T-sensor functioning as a reference between both panels. In Fig. 7a, the entire 152-m range is covered. In Fig. 7b, spectra from data from all T-sensors in the lower h ≤ 4.4 m above the seafloor are presented. In that panel also band-pass filter ranges are indicated by color bars for use in Figs. 8–9.

In both panels of Fig. 7, spectral slopes are plotted as black-dashed lines (on the log-log plots) and which represent in unscaled plots: ω^{-2} for general internal wave spectra outside inertial, tidal (harmonic) and buoyancy frequencies (Garrett and Munk, 1972) but also for fine-structure contamination (Phillips, 1971; Reid, 1971), $\omega^{-5/3}$ for the inertial subrange of turbulence predominantly induced by shear and representing passive scalars (Tennekes and Lumley, 1972; Warhaft, 2000), and $\omega^{-7/5}$ for turbulence predominantly induced by buoyancy-driven convection and representing active scalars (Bolgiano, 1959; Pawar and Arakeri, 2016). The steepest slope of $\omega^{-7/3}$ is merely a fit to the high-frequency internal wave/low-frequency turbulence part of the buoyancy subrange of the spectrum. For shortening, below we will designate spectral slopes (in log-log plot) by their exponent only, e.g., −7/3-slope.

Although the inertial subrange $\omega > \omega_O$ is modelled as the equilibrium range between shear-driven turbulence input at large scales and dissipation at small scales (Kolmogorov, 1941; Obukhov, 1949; Ozmidov, 1965) for a passive scalar (Tennekes and Lumley, 1972; Warhaft, 2000), the range $\omega < \omega_O$, including the spectral dip and the −7/5-slope, has various naming. While understood as a buoyancy subrange containing the larger anisotropic eddies directly influenced by the density stratification (Bolgiano, 1959) or stratified turbulence (Bouruet-Aubertot et al., 2010), (part of) it is also indicated as the internal wave range (Garrett and Munk, 1972), (part of) internal swash and turbulent production range (Polzin et al., 2021), while the deviations from the −5/3-slope such as the −7/5-slope are indicated as that representing an active scalar (Pawar and Arakeri, 2016) evidencing buoyancy-driven convection-turbulence.

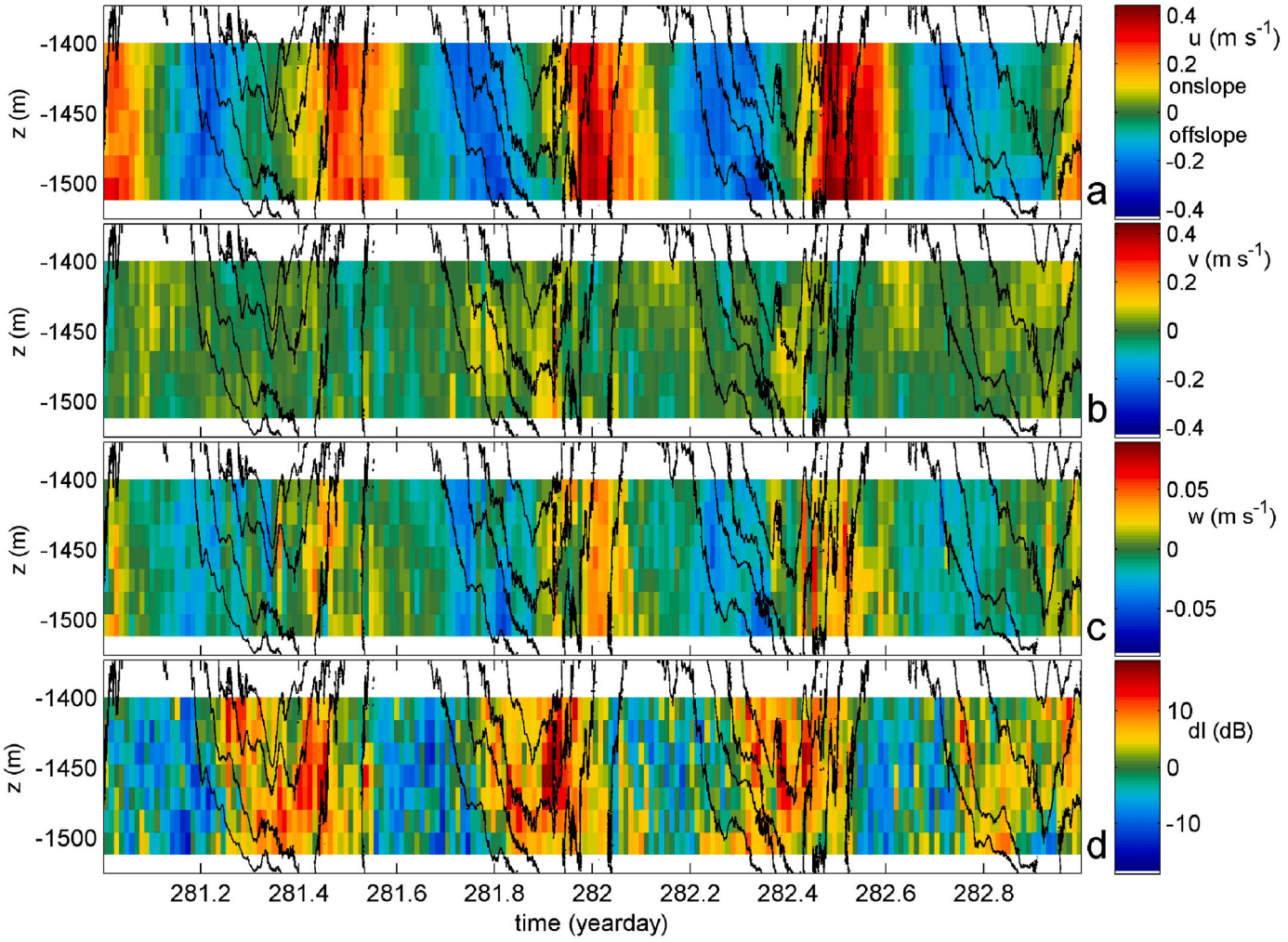

Fig. 5. As Fig. 4 including the black isotherms for reference, but for 900 s sampled current and acoustic measurements by ADCP smoothed vertically over 2 bins for display purposes. The lower 10 m above the seafloor did not provide useful data due to side-lobe contamination. (a) Along-canyon current component. (b) Cross-canyon current component. (c) Vertical current component with different colour-scale compared to a.,b. (d) Acoustic echo amplitude relative to time mean values.

Vertical black lines indicate boundary frequencies associated with internal waves, turbulence, and instrumental noise. Internal waves associated with $\omega \in$ [f, (N_{min}) N (N_{max})], in which the upper bound may take any value between $N_{min} < N < N_{max}$, of which [f, N] is generally considered to mainly consist of undamped linear and unsaturated internal waves and $\omega > N$ to consist of damped nonlinear and saturated internal waves (Weinstock, 1978; Munk, 1981). Turbulence is found in various identities in the range $\omega \in$ [(N_{min}) … (N_{max}), ω_O, lpf], and instrumental noise is found at $\omega >$ lpf.

In Fig. 7a, it is seen that semidiurnal and higher harmonic motions at $\omega < N_{min}$ show increasing temperature variance further away from the seafloor, although the lower 10 m above the seafloor demonstrate small differences. This changes for $\omega > N_{min}$, which is the starting frequency of small temperature variance differences that progressively become larger with increasing frequency beyond tidal harmonic $M_{10} = 5M_2$ (fourth overtide of M_2). At $\omega = \omega_O$, the spread in variance is about maximum and more than one order of magnitude from h = 1–4 m. The bulk of this variance-spread is due to changes in the lower 2.5 m above the seafloor (Fig. 7b), as for $\omega > \omega_O$ and h > 3.4 m the spectra cluster together and (have) become horizontal at about the same variance.

At $\omega = N_{max}$, minimum (scaled) variance is observed at T-sensors for 2 < h < 30 m. In that height-range above the seafloor, the spectral slope towards this minimum is close to −2 for h < 5 m and tends to steeper values down to −7/3 at h = 0.9 m for $2N_{min} < \omega < N_{max}$. At $\omega > N_{max}$, either the spectral slope follows −7/5 going up in the scaled plot (for 1.5 < h < 30 m), remains more or less horizontal (for 30 < h < 75 m), or continues to slope like −2 before becoming horizontal (for h = 0.9 m and 75 < h < 152 m). The difference in slope-dependence is depicted in Fig. 7 for h = 5.4, 50 and 150 m, respectively. The slope-change between spectra at h = 10 and 50 m is small, and their intermediate spectra around h = 30 m are mostly horizontal between $N_{max} < \omega < \omega_O$. For h > 35 m the inertial subrange progressively slopes slightly and shifts to higher frequencies, being pushed by more variance in the small-scale thin-layer internal wave band $\omega < N_{max}$ (see, as an almost identical example for h > 100 m, the spectrum at h = 150 m in Fig. 7a, which also shows a horizontal $\omega^{-5/3}$-scaled level between $N_{min} < \omega < N$). The spectra start rolling off to instrumental noise around the frequency at which the lpf cut-off is chosen. The two peaks in the high-frequency portion are probably artificial and possibly reflect harmonics of vortex shedding or mooring rotations.

In the lower 5 m from the seafloor, more than one order of magnitude change in variance is observed at the lpf-frequency (Fig. 7b). Between (local) $N_{max} \sim< \omega \sim< \omega_O$, all (scaled) spectra increase in variance with frequency, except for the lowest T-sensor. The lowest T-sensor spectrum either slopes horizontal, i.e., like −5/3, or like −2. At the other four T-sensors, the slope is close to −7/5 before becoming −5/3 (sensors at h = 3.4 and 4.4 m) or continuing its −7/5-slope before rolling off to noise (at h = 1.4 and 2.4 m) without resolving an inertial subrange like at 0.9 m. With distance from the seafloor, a shift to lower frequencies is thus noted for both the frequency of the minimum variance level, i.e., transition

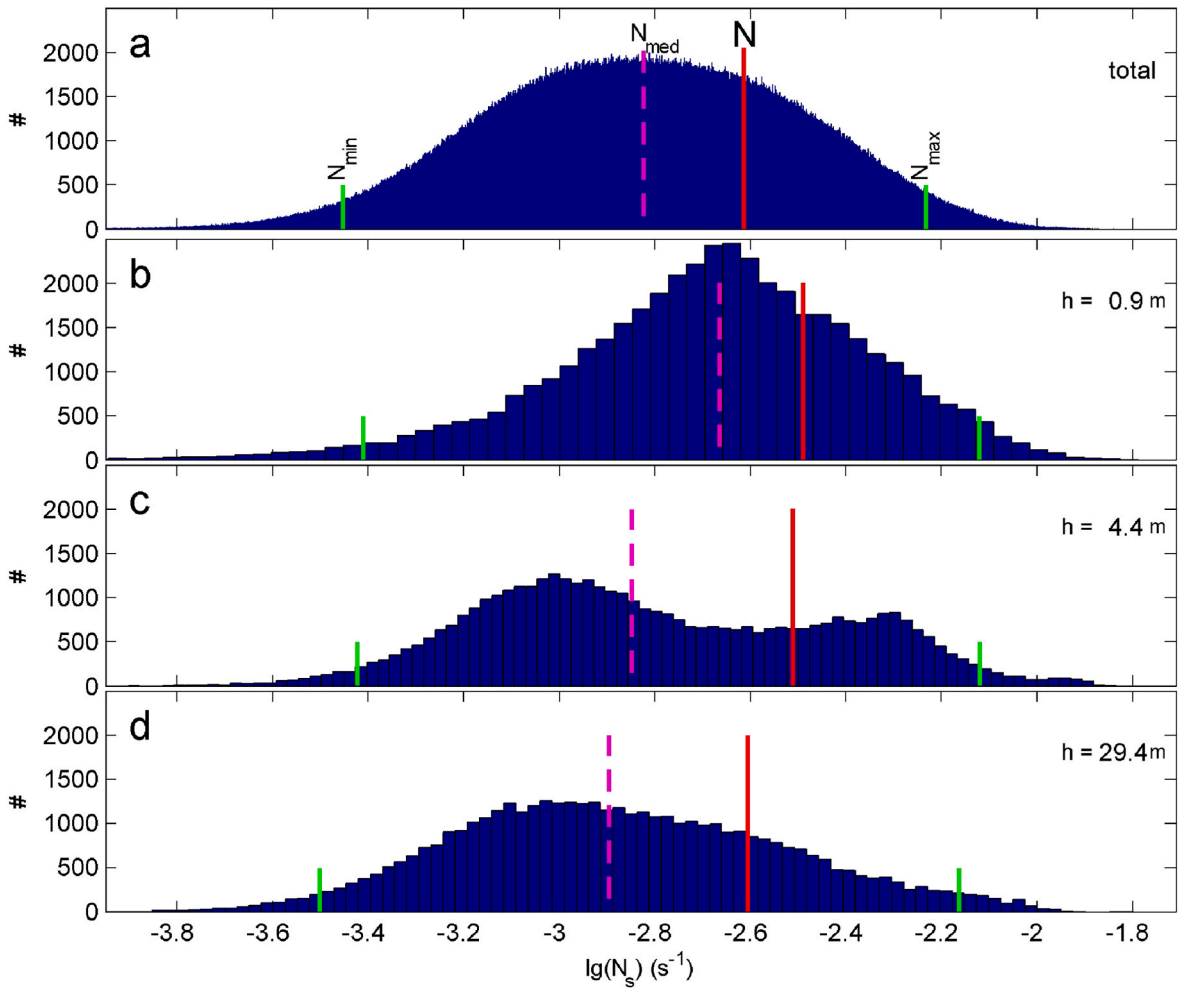

Fig. 6. Pdf's in #'s of occurrences of small-scale buoyancy frequencies of Fig. 4c, with in green 2.5% and 97.5% values indicated as N_{min} and N_{max}, respectively, and median value in dashed-purple and root-mean-square N in red. (a) Total for all 2-s sampled 2.07 day long 103T-sensors. (b) Lowest T-sensor, with h indicating the distance above the local seafloor. (c) Fifth sensor from the seafloor. (d) Thirtieth sensor from the seafloor.

from about −2 to −7/5-slope, and the transition from −7/5 to −5/3 slope. The frequency range of −7/5-slope is approximately constant and amounts about 1.5 orders of magnitude. The maximum level of inertial-subrange variance is reached at about h = 5.4 m while higher-up a minimum level is observed at about 50 m, both around the lpf-frequency (Fig. 7a).

The spectral 'dip' has been observed in spectra from towed temperature measurements, including a slope of −5/2 in the lower (wavenumber) range and −5/3 in the higher wavenumber range (Klymak and Moum, 2007), whereby deviations to −7/5-slope were not observed. This may be because those observations were not obtained very close, more than 50 m away, from sloping topography.

Dip-deepening with slope < -2 and dip-filling with convection-turbulence slope −7/5 has been observed in weakly stratified waters under breaking internal waves in Lake Garda (van Haren and Dijkstra, 2021). In our observations it is seen to reach very close to the seafloor, approximately from h = H_b = 30 m down to about h = 1.5 m, as inferred from the yearlong averaged spectra. This convection is unlikely dominated by geothermal heating, but here predominantly enforced by breaking internal waves. The lower 1 m shows a spectacular shift to lack of convection-turbulence slope or unresolved turbulence production. It shows the most explicit −7/3-slope between (2)$N_{min} < \omega < N_{max}$. This is as if the near-boundary lacks small-scale turbulence motions in a rather smooth 1-m thin layer above the seafloor, which is characterized by a non-lognormal small-scale buoyancy frequency distribution (Fig. 6b).

3.3. Two-day data revisited with focus just above the seafloor

For a single semidiurnal period around local (internal) springs, temperature variations are split in four portions using different band-pass filters for: the large-scale internal wave band (1–5 cpd), the small-scale high-frequency internal wave band and large-scale turbulence buoyancy subrange (10–100 cpd), the small-scale buoyancy subrange including convection-turbulence for 1 < h < 30 m and inertial subrange higher up (100–1000 cpd), and the inertial subrange (1500–4000 cpd). For simplicity, linear band pass filters are used on strongly nonlinear processes. These frequency ranges follow from the spectral observations in Fig. 7. To focus near the seafloor, the vertical scale of the time-depth magnification is plotted logarithmically (Fig. 8).

In original temperature (Fig. 8a), it is seen that cold periods reach up to about h = 30 m, lg (30) = 1.48, while the warming reaches down to about the same height, except for a short period of <2 h which includes the transition from warming to cooling, considerable convection from above and an upslope propagating turbulent bore, if existent. In the low-frequency internal wave band (Fig. 8b) variations are mostly linear with a distinct broadening of the warming phase towards the seafloor. Although these filtered data are clearly not steepened enough to be named internal swash (Polzin et al., 2021) which may be more appropriate for the full data in Fig. 8a as suggested by Emery and Gunnerson (1973), but to which we note that a back-wash is seldom observed, higher harmonics are required to deviate the narrow internal wave band

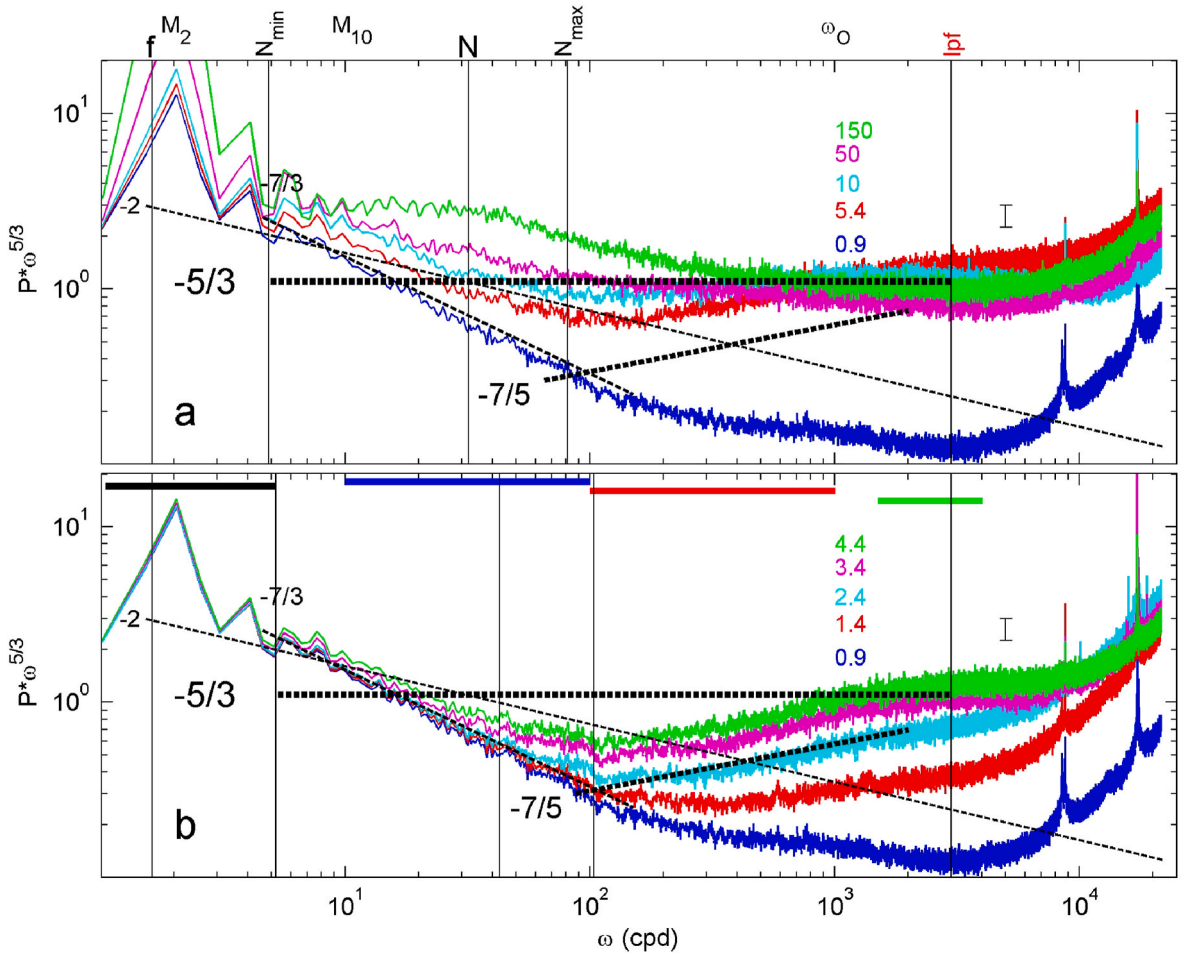

Fig. 7. Strongly smoothed (about 300 degrees of freedom) temperature variance of power P frequency (ω) spectra focusing on the turbulence range and scaled with the inertial subrange slope $\omega^{-5/3}$, for 400-day data from vertical levels as indicated by their height h(m) above the seafloor. Several frequencies (see text) are indicated with vertical lines, except for semidiurnal tidal M_2, higher harmonic M_{10} and Ozmidov frequency ω_O. Four spectral slopes are indicated by dashed black lines and their exponent (for unscaled log-log plots). (a) Covering the entire range of observations. (b) Focusing on the lower 5 T-sensors. The horizontal colour bars indicate various band-pass filter ranges used in Figs. 8–9.

from pure linear waves, which results in shorter period warming and longer period cooling phases. In the buoyancy range of combined internal wave band and stratified turbulence $2N_{min} < \omega < N_{max}$ (Fig. 8c), the level of h = 30 m marks a clear transition between abundant high-frequency variability throughout the record above, and a lower layer that is rather limited to low-frequency variability between days 281.8 and 282.1. Variability seems to stick to temperature contours and goes all the way to h = 0.9 m. Quite different is the high-frequency part of the buoyancy subrange or convection-turbulence subrange $N_{max} < \omega < \omega_O$ (Fig. 8d), with yet considerable variability down to about h = 4 m, lg (4) = 0.6, and distinct loss of variability towards the seafloor. The convection in this subrange is observed in the broad time-period between days 281.82 and 282 covering the warming to cooling phases, with most internal wave variability around the mean buoyancy frequency (Fig. 8c), and briefly during the cold phase around day 282.08. Further reduction in variance is observed in the inertial subrange (Fig. 8e), with a sharp decrease in the lower three T-sensor levels at h < 3 m, lg (3) = 0.5, and most limited variability at the lowest T-sensor. Over a semidiurnal period, the lowest T-sensor shows hardly any inertial subrange variability during the warming phase, and some when cold water goes upslope during the cooling phase, frontal passage, and cold phase, related with a secondary front (van Haren et al., 2022a).

The difference or correspondence between the three frequency bands and three tidal phases is depicted as vertical profiles in Fig. 9 for the two-day spring-tide period of Fig. 4. While internal-wave temperature standard deviation (std; square-root of variance within a frequency band) has a maximum at about h = 100 m, its profile steadily decreases in value for h < 35 m (Fig. 9a). This decrease is also found in convection-turbulence subrange variance, but not in inertial subrange variance which steadily increases towards the seafloor before abruptly decreasing in value for h < 5 m.

Two-day representative profiles for turbulence values are computed as total-means and ensemble averages over three 2-h intervals during warming, cooling, and cold tidal phases (defined in Fig. 8a). The turbulence dissipation rate (Fig. 9b) and turbulence diffusivity (Fig. 9c) show very similar profiles, with total-means varying over one order of magnitude with a slight bulge between h = 50 and 90 m, and an increase for h < 5 m. Such increases near the seafloor are observed to occur for the cooling and cold tidal phases, but not for the warming phase which shows a sharp decrease to an overall minimum value. While the cooling phase shows a maximum at mid-range, such is not observed in the cold-phase profile that is most constant over the vertical. This observed difference between different tidal phases in vertical turbulence profiles with special attention in the lower few meters above the sloping seafloor has been noted before for turbulence diffusivity by van Haren and Gostiaux (2012). For completeness, the associated vertical profiles for buoyancy frequency are given in Fig. 9d, showing an increase in value for h < 1.5 m, for every profile.

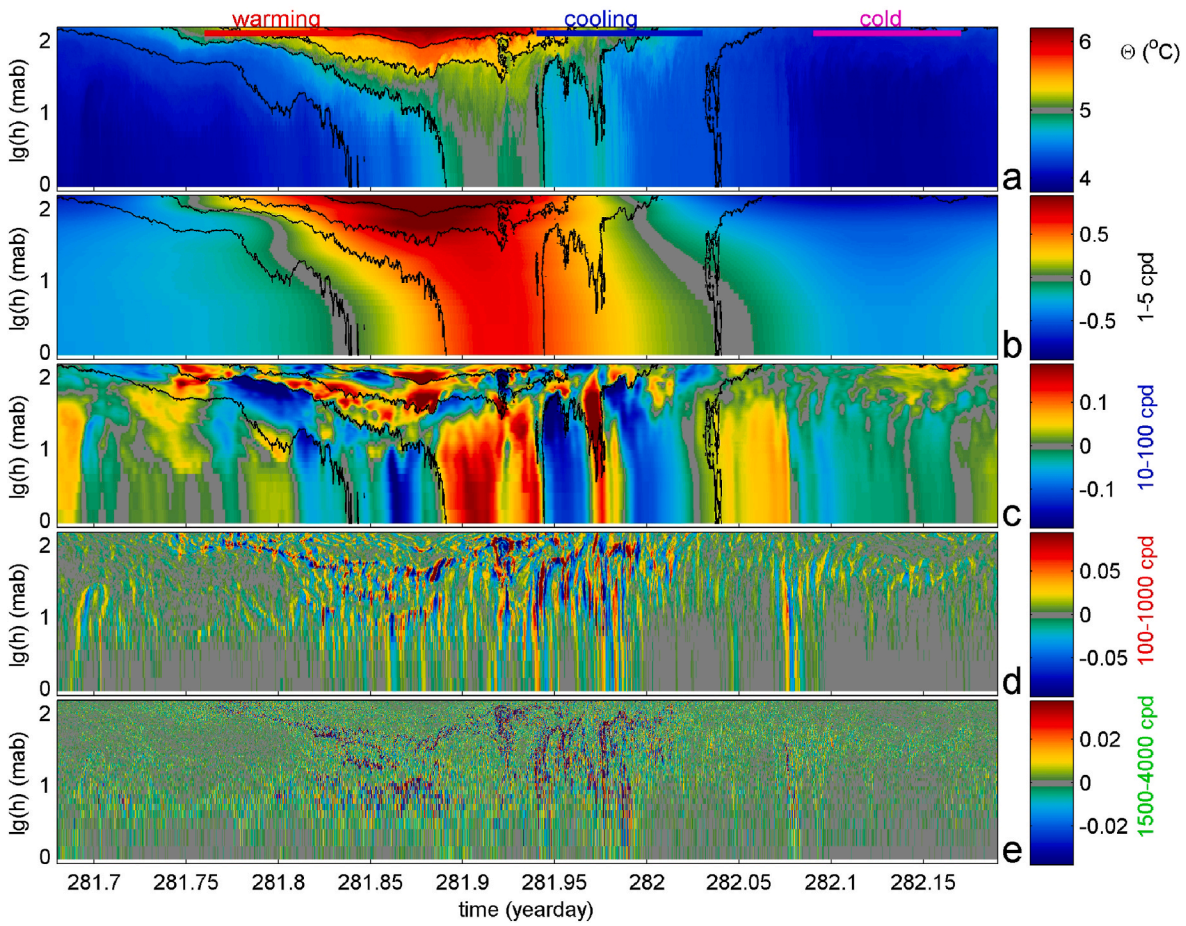

Fig. 8. One semidiurnal period from Fig. 4a but plotted with the logarithm of the vertical distance h from the seafloor for 2-s sampled data, together with four different band-pass filtered data of which the ranges are indicated, also by colour bars in Fig. 7b. Note that the horizontal axes are not at the seafloor. (a) Conservative Temperature with 3 bars indicating various 2-h-period phases of an internal tidal period (see text). (b) Data from a., band-pass filtered for the low-frequency internal wave range. (c) As b., but for the high-frequency internal wave/low-frequency stratified turbulence range. Note the different colour scale compared with b. (d) As c., but for the high-frequency stratified turbulence range. (e) As c., but for the inertial subrange throughout the T-sensor range.

4. Discussion

The yearlong monitoring of temperature variations in the lower 150 m above the seafloor and the calculation of turbulence values using the method of sorting the high-resolution temperature data down to 1 m from the seafloor, yielded an overall weak increase of relatively high turbulence values with increasing depth. The turbulence is dominated by the braking of semidiurnal internal tides. A strong distinction is found in the lower 1–5 m above the seafloor, in which temperature variance decreases, but turbulence values increase with depth by almost an order of magnitude. Apart from the lowest sensor at 0.9 m that did not register much convection and inertial subrange, a distinct buoyancy subrange is found between 1 and 5 m above the seafloor. Further up, shear dominates the spectral turbulence subrange. It is hypothesized that the lack of a mean near-seafloor buoyancy-flux reduction that may govern along-canyon up-welling is compensated by 3D-effects such as affecting non-tidal flow-deformation off-setting near-seafloor turbulence reduction (Jagannathan et al., 2023), an extremely thin layer <0.9 m, temporary effects such as during the warming phase of the tide, less steep slope effects, or none of these.

If we follow the parametrization by Bouruet-Aubertot et al. (2010), and extrapolate the observed large-100-m-scale correspondence between (partial) turbulence inertial-subrange level in [1500, 4000]cpd and mean turbulence dissipation rate, only a very thin, less than a few meters, layer above the seafloor would result in which turbulence may potentially be reduced. In that case, the requirement for up-welling along sloping boundaries to compensate for down-welling in the ocean interior following a reduction of turbulent buoyancy flux with depth, as suggested in 2D by Ferrari et al. (2016), would be restricted to a very limited layer above sloping seafloors. However, we observed in the lower 1–5 m above the sloping seafloor that the above general correspondence between two-day mean values of turbulence inertial subrange and dissipation rate switches to an inverse relationship, so that the reduction in inertial-subrange variance is observed to coincide with increase in turbulence dissipation rate. These observations confirm previous turbulent diffusivity profiles from above open slopes of a seamount (van Haren and Gostiaux, 2012).

Thus, if a reduction in turbulent buoyancy flux would occur as suggested for up-welling across a slope to compensate for down-welling in the ocean-interior (Ferrari et al., 2016), it does not associate with an Ekman layer O (10) m but with the log-layer $L \ll 1$ m, hence very limited in height. This is because the increase of turbulent buoyancy flux, calculated from overturning scales employing constant mixing efficiency of 0.2 over tidally averaged data, down to h = 1 m is not predominantly governed by (steady or oscillatory) frictional flows over the seafloor as in the Prandtl concept, but by the breaking of internal waves after nonlinear deformation due to the steeply sloping topography leading to large-scale convective plunging and overturning reaching the seafloor. The internal wave breaking above sloping topography also ensures rapid restratification making the turbulent mixing efficient, to within 1 m from the seafloor.

While turbulence values increase sharply in the lower 3 m from the

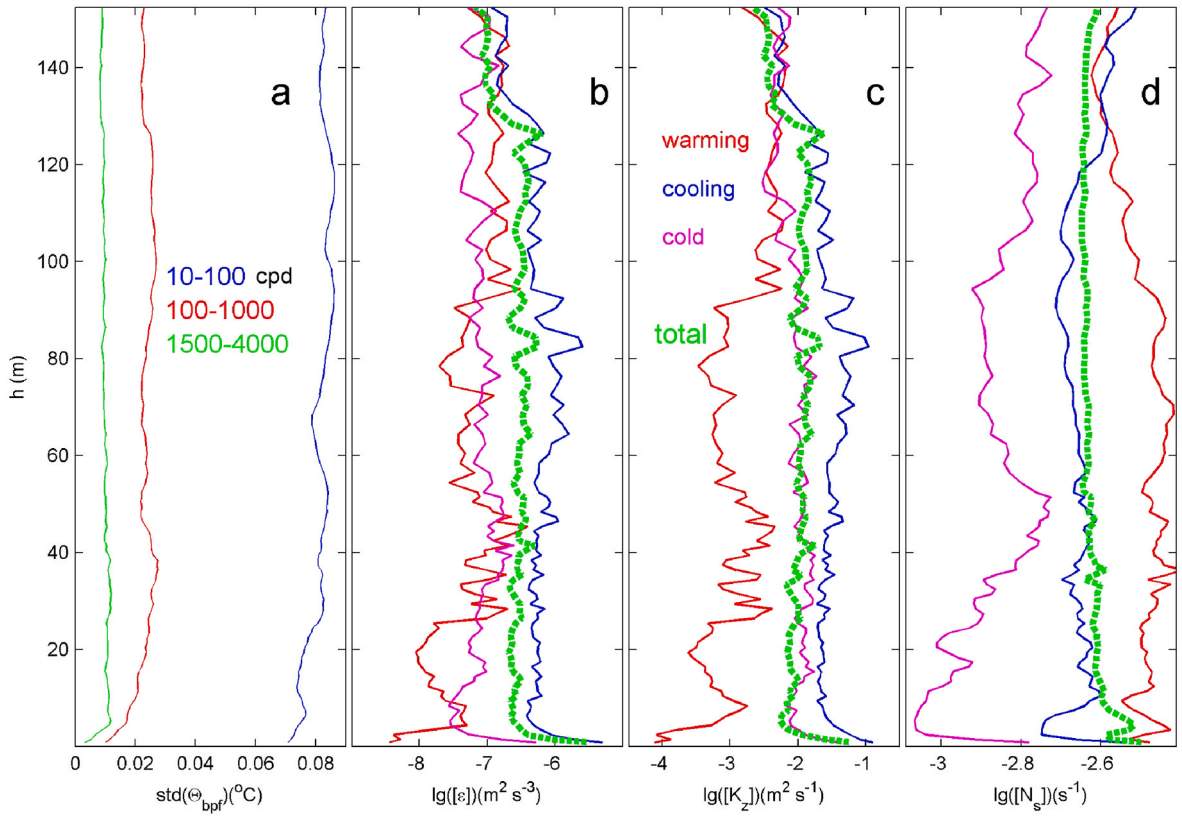

Fig. 9. Two-day mean profiles for 2-s sampled data from Fig. 4 as a function of height above the seafloor. (a) Band-pass filtered temperature std, with indicated filter ranges (see also Fig. 7b). (b) Logarithm of turbulence dissipation rate with x-axis range over 5 orders of magnitude, with total 2-d mean (green-dashed) and the means of four 2-h periods during tidal phases of (cf. Fig. 8a): warming, cooling immediately after frontal bore passage over the seafloor by upslope flow, and cold around the transition from cooling to warming. (c) As b., but for turbulence diffusivity with x-axis range over 4 orders of magnitude. (d) As b., but for small-scale buoyancy frequency with x-axis-range over <1 order of magnitude.

seafloor, temperature-variance decreases. Over the same small vertical distance, the distribution of small-scale stratification changes significantly from a lognormal distribution, as is found for $h > 30$ m, with a dual-peaked distribution to large and small values in thin and thick layers respectively, except in the lowest 1 m. The observed non-lognormal peaking at interior large-scale N close to the seafloor at $h = 0.9$ m and the spread to thin and thick layers in the few meters above, $1 < h < 3$ m, suggests strong restratification of the breaking waves coming from the interior stratification. Such restratification following sloshing up- and down a slope has been associated with bores that appear during certain phases of the carrier wave (Emery and Gunnerson, 1973; Winters, 2015).

In the frequency domain, the discrepancy in the lower 1 m manifests as a steep −7/3-slope in the internal wave band and a lack of both convection-turbulence and shear-turbulence. This has some comparison with a seafloor being heated from below, in which convection in up- and down-going plumes does not actually touch the boundary but starts some distance above at the top $3z_0$ of the conduction layer (Townsend, 1959), z_0 defined below, from which it intermittently forms convection plumes up to a height O (10 m) (Foster, 1971). In the present observations however, geothermal heating is not expected to be more important in turbulence generation than internal wave breaking, which may cause convection from above (van Haren and Dijkstra, 2021).

Scale-height computations for such non-convective layer under convection yield ambiguous results. Townsend (1959)'s scale height $3z_0 = (\kappa_T^3/gB)^{1/4} \approx 0.002$ m, while $\delta = (\pi\kappa_T t_*)^{1/2} = 0.03$ m (Howard, 1966) that may grow for a time scale of $t_* \approx 10\ (\nu/B)^{1/2} \approx 1800$ s. Here, variables include thermometric conductivity or molecular diffusivity $\kappa_T = 1.4 \times 10^{-7}$ m^2 s^{-1}, kinematic viscosity $\nu = 10^{-6}$ m^2 s^{-1}, acceleration of gravity $g = 9.81$ m s^{-2} and buoyancy flux $B = 3.2 \times 10^{-11}$ m^2 s^{-3} from local general geothermal heat flux $Q = 0.08$ W m^{-2} (Davies and Davies, 2010). If so, the lack of convection in spectra from T-sensor at $h = 0.9$ m may be associated with the log-layer reduction by geothermal heating of convection underneath internal waves breaking from above to $\delta = h$, requiring either a time-scale of $t_* = 21$ days, which seems unrealistically large, or a replacement of κ_T by a turbulent diffusivity of $K_z = 1.4 \times 10^{-4}$ m^2 s^{-1}, which seems feasible.

Resuming, the (re) stratifying 'boundary layer' of up- and down-slope sloshing of highly nonlinear internal waves thus consists of a 1-m thin non-convective layer but with high turbulence values (that matches a lack of T-variance), underneath a layer $1 < h < 2.5$ m of dominant convection-turbulence and relatively low temperature variance underneath internal waves, with progressively less convection- and more shear-turbulence with distance from the seafloor for $2.5 < h < 30$ m $\approx H_b$, above which shear-turbulence dominates exclusively for $h > 30$ m.

Separators in the frequency range include the 2.5% minimum buoyancy frequency at which nonlinearity becomes important and higher-frequency spectral slopes start to deviate, the 2.5% maximum buoyancy frequency at which a local dip is found in spectra from $1 < h < 30$ m, and the Ozmidov frequency at which all spectra tend to inertial subrange slope except for $h < 2.5$ m. These observations were clear in smooth well-resolved 400-day mean spectra but appeared already in spectra from less than two days of measurements. This provides consistency to the observations, even though every internal tidal cycle has a different appearance with different nonlinearity and different turbulence values.

It is questioned whether the spectral consistency is a reflection of the source, the internal tide, in the thalweg-enforced along-canyon flow component. The semidiurnal internal tidal flow is relatively well

determined, and so seems its higher harmonic deformation that appears phase-locked to its source. This local phase-locking may explain the consistency of the spectral observations. As the mooring was essentially one-dimensional, not counting time as dimension, unknown effects are due to wave-reflection off the canyon-sidewalls and the three-dimensionality of flows. Such effects may be essential for up-welling flow given that 1D (2D)-models (Ferrari et al., 2016) require a reduction of turbulent buoyancy flux towards the thalweg-seafloor, which is not observed. Recall that such lack of turbulent-flux reduction is found in tidally (all phases) averaged profiles.

However, as was previously observed above a Great Meteor Seamount slope in turbulent diffusivity profiles (van Haren and Gostiaux, 2012), the present turbulence-value profiles including those of buoyancy flux (∝ turbulence dissipation rate using constant mixing efficiency and four tidal-period averaging) show temporary lower values towards the seafloor during the warming tidal phase. The reduction by more than one order of magnitude (in 2-h averaged values) is observed for h < 4 m. Thus, for brief moments during a tidal cycle a thin layer of up-welling flow may be generated that is not hypsometry related (Kunze et al., 2012). Likewise, we recall that from repeated CTD-observations above a shallow water slope Emery and Gunnerson (1973) estimated that during 40% of a tidal cycle no effect of a sloping bottom was noticed like during the warming phase in present data, while during the remaining 60% either restratification occurred or internal wave breaking.

Thus, although up-welling cannot be inferred from tidally averaged profiles of buoyancy flux at a single location in the thalweg, temporary and 3D-effects are hypothesized to combine and may explain dye-experiments deeper in the canyon that suggest net up-welling flows (Wynne-Cattanach et al., 2024). Ongoing analysis of other observations in the canyon will therefore address the tidal phasing of the up-welling. This suggests nonlinear processes should not be under-estimated.

CRediT authorship contribution statement

Hans van Haren: Conceptualization, Data curation, Formal analysis, Investigation, Writing – original draft. **Gunnar Voet:** Investigation, Writing – review & editing. **Matthew H. Alford:** Conceptualization, Funding acquisition, Writing – review & editing. **Bieito Fernández-Castro:** Conceptualization, Writing – review & editing. **Alberto C. Naveira Garabato:** Conceptualization, Funding acquisition, Writing – review & editing. **Bethan L. Wynne-Cattanach:** Investigation, Writing – review & editing. **Herlé Mercier:** Conceptualization, Writing – review & editing. **Marie-José Messias:** Conceptualization, Writing – review & editing.

Declaration of competing interest

The authors declare the following financial interests/personal relationships which may be considered as potential competing interests:

Matthew Alford reports was provided by University of California San Diego Scripps Institution of Oceanography.

Data availability

Data will be made available on request.

Acknowledgements

We thank the captain and crew of the RRS Discovery and engineers from the Multiscale Ocean Dynamics Group at Scripps Institution of Oceanography for their assistance during mooring deployment and recovery and NIOZ-MRF for mooring preparation. This study was in part funded by the National Science Foundation under grant OCE-1756264. NIOZ temperature sensors have been funded in part by NWO, the Netherlands organization for the advancement of science.

Appendix A. Turbulence values calculated from moored T-sensors

Given the reasonably tight density-temperature relationship, the number of moored T-sensors and their spacing of 0.5–2.0 m, in combination with their low noise level and precision, allows for accurately calculating values of turbulence dissipation rate ε and K_z via the reordering of unstable overturns making vertical density-profiles statically stable (Thorpe, 1977). These overturns follow reordering every 2 s the 152-m high potential density (Conservative Temperature) profile $\sigma_2(z)$, which may contain unstable inversions, into a stable monotonic profile σ_2 (z_s) without inversions. After comparing observed and reordered profiles, displacements $d = \min(|z\text{-}z_s|)\cdot\mathrm{sgn}(z\text{-}z_s)$ are calculated necessary to generate the reordered stable profile. Test-thresholds are applied to disregard apparent displacements associated with instrumental noise and post-calibration errors (Galbraith and Kelley, 1996). Such a test-threshold is very low $<5 \times 10^{-4}$°C for original sampled non-spiked NIOZ T-sensor data. Otherwise, identical methodology is used as proposed in Thorpe (1977) and used in, e.g., Levine and Boyd (2006); Aucan et al. (2006); Nash et al. (2007), see van Haren and Gostiaux (2012) for details. It includes a constant mixing efficiency of 0.2 (Osborn, 1980; Oakey, 1982), an Ozmidov scale $L_O = (\varepsilon/N^3)^{0.5}$ (Dougherty, 1961; Ozmidov, 1965) – root-mean-square (rms) overturn scale $d_{rms} = (1/n\ \Sigma d^2)^{0.5} = L_T$ ratio of $L_O/L_T = 0.8$ (Dillon, 1982) over many-n samples and the computation of local small-scale buoyancy frequency $N_s(t,z)$ from the reordered stable density (temperature) profiles (Thorpe, 1977; Dillon, 1982). Although individual values of mixing efficiency vary over at least an order of magnitude (Oakey, 1982; Dillon, 1982), moored T-sensor data allow for sufficient averaging to warrant the use of overturning and constant mixing efficiency in the computation of turbulence values. When sufficient averaging over time and/or depth is applied, various types, conditions and stages of turbulence are included, each with different efficiency (Mater et al., 2015). Large-scale overall mean N is computed as rms (N_s), a linear operation as $N^2 \propto d\sigma_2/dz$. Then, using d rather than d_{rms} as explained below,

$$\varepsilon = 0.64 d^2 N_s^3, \tag{A.1}$$

$$K_z = 0.2 \varepsilon N_s^{-2}. \tag{A.2}$$

In (A.1), and thus (A.2), individual d replace their rms-value across a single overturn as originally proposed by Thorpe (1977). The reason is that individual overturns cannot easily be distinguished, because overturns are found at various scales with small ones overprinting larger overturns, as one expects from turbulence.

This procedure provides high-resolution time-vertical images of turbulence values, for qualitative studies. Subsequently for quantitative studies, 'mean' turbulence values are calculated by arithmetic averaging over the vertical $< \ldots >$ or over time [.], or both, which is possible using moored high-resolution T-sensors (van Haren, 2017). This ensures the sufficient averaging required to use the above mean constant values (e.g., Osborn, 1980; Oakey, 1982; Mater et al., 2015; Gregg et al., 2018).

Using similar moored T-sensor data from Great Meteor Seamount, van Haren and Gostiaux (2012) found turbulence values to within a factor of three like those inferred from ship-borne CTD/LADCP profiler data using a shear/strain parameterisation near the seafloor. Their values compare well

with microstructure profiler-based estimates in similar sloping topography areas by Klymak et al. (2008). Comparison between calculated turbulence values using shear measurements and using overturning scales with $L_O/d_{rms} = 0.8$ from areas with such mixtures of turbulence development above sloping topography led to consistent results (Nash et al., 2007), after suitable averaging over the buoyancy scales. Thus, from the argumentation above and the reasoning in Mater et al. (2015), internal wave breaking is unlikely to bias turbulence dissipation rates computed from overturning scales by more than a factor of two to three, provided some suitable time-space averaging is done instead of considering single profiles. This is within the range of error, also of general ocean turbulence measurements (Oakey, 1982).

Appendix B. Figure B1

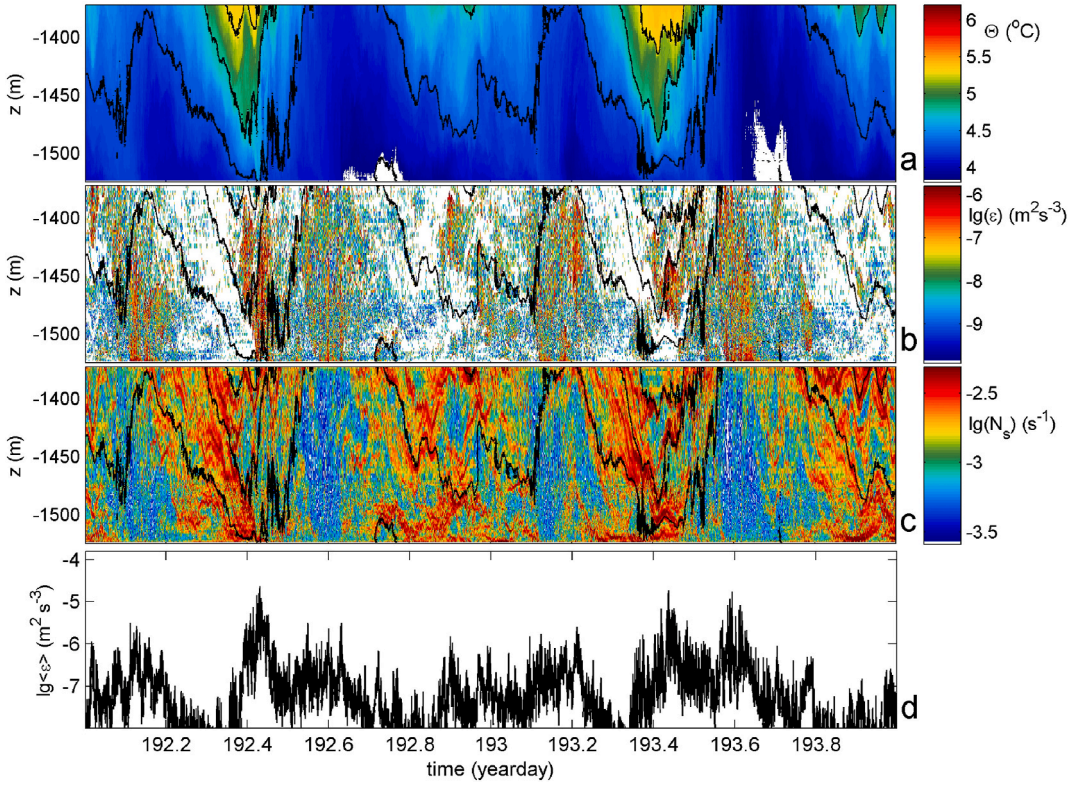

Fig. B1. As Fig. 4, but for period approximately around neap tide near the start of the mooring period.

References

Alford, M.H., Pinkel, R., 2000. Observations of overturning in the thermocline: the context of ocean mixing. J. Phys. Oceanogr. 30, 805–832.

Anderson Jr., J.D., 2005. Ludwig Prandtl's boundary layer. Phys. Today 58 (12), 42–48.

Armi, L., 1978. Some evidence for boundary mixing in the deep ocean. J. Geophys. Res. 83, 1971–1979.

Armi, L., 1979. Effects of variations in eddy diffusivity on property distributions in the oceans. J. Mar. Res. 37, 515–530.

Aucan, J., Merrifield, M.A., Luther, D.S., Flament, P., 2006. Tidal mixing events on the deep flanks of Kaena Ridge, Hawaii. J. Phys. Oceanogr. 36, 1202–1219.

Bolgiano, R., 1959. Turbulent spectra in a stably stratified atmosphere. J. Geophys. Res. 64, 2226–2229.

Bouruet-Aubertot, P., van Haren, H., LeLong, M.-P., 2010. Stratified inertial subrange inferred from in situ measurements in the bottom boundary layer of Rockall Channel. J. Phys. Oceanogr. 40, 2401–2417.

Brink, K.H., Lentz, S.J., 2010. Buoyancy arrest and bottom Ekman transport. Part II: oscillating flow. J. Phys. Oceanogr. 40, 636–655.

Davies, J.H., Davies, D.R., 2010. Earth's surface heat flux. Solid Earth 1, 5–24.

de Lavergne, C., Madec, G., Le Sommer, J., Nurser, A.J.G., Naveira Garabato, A.C., 2016. On the consumption of Antarctic Bottom Water in the abyssal ocean. J. Phys. Oceanogr. 46, 635–661.

Dillon, T.M., 1982. Vertical overturns: a comparison of Thorpe and Ozmidov length scales. J. Geophys. Res. 87, 9601–9613.

Dougherty, J.P., 1961. The anisotropy of turbulence at the meteor level. J. Atmos. Terr. Phys. 21, 210–213.

Drake, H.F., Ruan, X., Callies, J., Ogden, K., Thurnherr, A.M., Ferrari, R., 2022. Dynamics of eddying abyssal mixing layers over sloping rough topography. J. Phys. Oceanogr. 52, 3199–3219.

Emery, K.O., Gunnerson, C.G., 1973. Internal swash and surf. Proc. Natl. Acad. Sci. USA 70, 2379–2380.

Eriksen, C.C., 1982. Observations of internal wave reflection off sloping bottoms. J. Geophys. Res. 87, 525–538.

Ferrari, R., Mashayek, A., McDougall, T.J., Nikurashin, M., Campin, J.-M., 2016. Turning ocean mixing upside down. J. Phys. Oceanogr. 46, 2239–2261.

Flores, O., Riley, J.J., 2011. Analysis of turbulence collapse in the stably stratified surface layer using direct numerical simulation. Bound.-Layer Meteor. 139, 241–259.

Foster, T.D., 1971. Intermittent convection. Geophys. Fluid Dynam. 2, 201–217.

Galbraith, P.S., Kelley, D.E., 1996. Identifying overturns in CTD profiles. J. Atmos. Ocean. Technol. 13, 688–702.

Garrett, C., 1990. The role of secondary circulation in boundary mixing. J. Geophys. Res. 95, 989–993.

Garrett, C., Munk, W., 1972. Space-time scales of internal waves. Geophys. Fluid Dynam. 3, 225–264.

Gregg, M.C., D'Asaro, E.A., Riley, J.J., Kunze, E., 2018. Mixing efficiency in the ocean. Ann. Rev. Mar. Sci 10, 443–473.

Hall, R.A., Carter, G.S., 2011. Internal tides in Monterey submarine canyon. J. Phys. Oceanogr. 41, 186–204.

Holleman, R.C., Geyer, W.R., Ralston, D.K., 2016. Stratified turbulence and mixing efficiency in a salt wedge estuary. J. Phys. Oceanogr. 46, 1769–1783.

Hosegood, P., Bonnin, J., van Haren, H., 2004. Solibore-induced sediment resuspension in the faeroe-shetland channel. Geophys. Res. Lett. 31, L09301 https://doi.org/10.1029/2004GL019544.

Howard, L.N., 1966. Convection at high Rayleigh number. In: Görtler, H. (Ed.), Applied Mechanics. Springer, Berlin, pp. 1109–1115.

IOC, SCOR, IAPSO, 2010. The International Thermodynamic Equation of Seawater – 2010: Calculation and Use of Thermodynamic Properties. Intergovernmental Oceanographic Commission, Manuals and Guides No. 56. UNESCO, Paris, France, pp. 1–196.

Jagannathan, A., Srinivasan, K., McWilliams, J.C., Molemaker, J., Stewart, A.L., 2023. Evolution of bottom boundary layers on three dimensional topography—buoyancy adjustment and instabilities. J. Geophys. Res. 128, e2023JC019705.
Klymak, J.M., Moum, J.N., 2007. Oceanic isopycnal slope spectra. Part II: turbulence. J. Phys. Oceanogr. 37, 1232–1245.
Klymak, J.M., Pinkel, R., Rainville, L., 2008. Direct breaking of the internal tide near topography: kaena Ridge, Hawaii. J. Phys. Oceanogr. 38, 380–399.
Kolmogorov, A.N., 1941. The local structure of turbulence in incompressible viscous fluid for very large Reynolds numbers. Dokl. Akad. Nauk SSSR 30, 301–305.
Kunze, E., MacKay, C., McPhee-Shaw, E.E., Morrice, K., Girton, J.B., Terker, S.R., 2012. Turbulent mixing and exchange with interior waters on sloping boundaries. J. Phys. Oceanogr. 42, 910–927.
LeBlond, P.H., Mysak, L.A., 1978. Waves in the Ocean. Elsevier, New York, USA.
Levine, M., Boyd, T.J., 2006. Tidally forced internal waves and overturns observed on slope: results from HOME. J. Phys. Oceanogr. 36, 1184–1201.
Lozovatsky, I., Wainwright, C., Creegan, E., Fernando, H.J.S., 2021. Ocean Turbulence and mixing near the shelf break south-east of Nova Scotia. Bound.-Layer Meteor 181, 425–441.
MacCready, P., Rhines, P.B., 1991. Buoyant inhibition of Ekman transport on a slope and its effect on stratified spin-up. J. Fluid Mech. 223, 631–661.
Mater, B.D., Venayagamoorthy, S.K., St Laurent, L., Moum, J.N., 2015. Biases in Thorpe scale estimates of turbulence dissipation. Part I: assessments from large-scale overturns in oceanographic data. J. Phys. Oceanogr. 45, 2497–2521.
McDougall, T.J., Ferrari, R., 2017. Abyssal up-welling and down-welling driven by near-boundary mixing. J. Phys. Oceanogr. 47, 261–283.
Munk, W.H., 1966. Abyssal recipes. Deep-Sea Res. 13, 707–730.
Munk, W.H., 1980. Internal wave spectra at the buoyant and inertial frequencies. J. Phys. Oceanogr. 10, 1718–1728.
Munk, W., 1981. Internal waves and small-scale processes. In: Warren, B.A., Wunsch, C. (Eds.), Evolution of Physical Oceanography. MIT Press, Cambridge, MA, USA, pp. 264–291.
Munk, W., Wunsch, C., 1998. Abyssal recipes II: energetics of tidal and wind mixing. Deep-Sea Res. I 45, 1977–2010.
Nash, J.D., Alford, M.H., Kunze, E., Martini, K., Kelly, S., 2007. Hotspots of deep ocean mixing on the Oregon. Geophys. Res. Lett. 34, L01605 https://doi.org/10.1029/2006GL028170.
New, A.L., Smythe-Wright, D., 2001. Aspects of the circulation in the Rockall trough. Continent. Shelf Res. 21, 777–810.
Oakey, N.S., 1982. Determination of the rate of dissipation of turbulent energy from simultaneous temperature and velocity shear microstructure measurements. J. Phys. Oceanogr. 12, 256–271.
Obukhov, A.M., 1949. Structure of the temperature field in a turbulent flow. Izv. Akad. Nauk SSSR, Ser. Geogr. Geofiz. 13, 58–69.
Osborn, T.R., 1980. Estimates of the local rate of vertical diffusion from dissipation measurements. J. Phys. Oceanogr. 10, 83–89.
Ozmidov, R.V., 1965. About some peculiarities of the energy spectrum of oceanic turbulence. Dokl. Akad. Nauk SSSR 161, 828–831.
Pawar, S.S., Arakeri, J.H., 2016. Kinetic energy and scalar spectra in high Rayleigh number axially homogeneous buoyancy driven turbulence. Phys. Fluids 28, 065103.
Phillips, O.M., 1971. On spectra measured in an undulating layered medium. J. Phys. Oceanogr. 1, 1–6.
Polzin, K.L., Wang, B., Wang, Z., Thwaites, F., Williams III, A.J., 2021. Moored flux and dissipation estimates from the northern deepwater Gulf of Mexico. Fluid 6, 237.
Reid, R.O., 1971. A special case of Phillips' general theory of sampling statistics for a layered medium. J. Phys. Oceanogr. 1, 61–62.
Ruan, X., Thompson, A.F., Taylor, J.R., 2019. The evolution and arrest of a turbulent stratified oceanic bottom boundary layer over a slope: downslope regime. J. Phys. Oceanogr. 49, 469–487.
Sarkar, S., Scotti, A., 2017. From topographic internal gravity waves to turbulence. Annu. Rev. Fluid Mech. 49, 195–220.
Smith, W.H.F., Sandwell, D.T., 1997. Global ocean-floor topography from satellite altimetry and ship depth soundings. Science 277, 1957–1962.
St Laurent, L.C., Toole, J.M., Schmitt, R.W., 2001. Buoyancy forcing by turbulence above rough topography in the Brazil Basin. J. Phys. Oceanogr. 31, 3476–3495.
Tennekes, H., Lumley, J.L., 1972. A First Course in Turbulence. The MIT Press, Boston, USA.
Thorpe, S.A., 1977. Turbulence and mixing in a Scottish loch. Phil. Trans. Roy. Soc. Lond. 286, 125–181.
Thorpe, S.A., 1987. Transitional phenomena and the development of turbulence in stratified fluids: a review. J. Geophys. Res. 92, 5231–5248.
Thurnherr, A.M., Clément, L., St Laurent, L., Ferrari, R., Ijichi, T., 2020. Transformation and up-welling of bottom water in fracture zone valleys. J. Phys. Oceanogr. 50, 715–726.
Townsend, A.A., 1959. Temperature fluctuations over a heated horizontal surface. J. Fluid Mech. 5, 209–241.
Ullgren, J.E., White, M., 2012. Observations of mesoscale variability in the Rockall trough. Deep-Sea Res. I 64, 1–8.
van Haren, H., 2015. Instability observations associated with wave breaking in the stable-stratified deep-ocean. Phys. D 292–293, 62–69.
van Haren, H., 2017. Exploring the vertical extent of breaking internal wave turbulence above deep-sea topography. Dynam. Atmos. Oceans 77, 89–99.
van Haren, H., 2018. Philosophy and application of high-resolution temperature sensors for stratified waters. Sensors 18, 3184. https://doi.org/10.3390/s18103184.
van Haren, H., Dijkstra, H.A., 2021. Convection under internal waves in an alpine lake. Environ. Fluid Mech. 21, 305–316.
van Haren, H., Gostiaux, L., 2012. Detailed internal wave mixing observed above a deep-ocean slope. J. Mar. Res. 70, 173–197.
van Haren, H., Oakey, N., Garrett, C., 1994. Measurements of internal wave band eddy fluxes above a sloping bottom. J. Mar. Res. 52, 909–946.
van Haren, H., Mienis, F., Duineveld, G., 2022a. Contrasting internal tide turbulence in a tributary of the Whittard Canyon. Continent. Shelf Res. 236, 104679.
van Haren, H., Voet, G., Alford, M.H., Torres, D.J., 2022b. Internal wave breaking near the foot of a steep East-Pacific continental slope. Prog. Oceanogr. 205, 102817.
Vlasenko, V., Stashchuk, N., Inall, M.E., Porter, M., Aleynik, D., 2016. Focusing of baroclinic tidal energy in a canyon. J. Geophys. Res. 121, 2824–2840. https://doi.org/10.1002/2015JC011314.
Warhaft, Z., 2000. Passive scalars in turbulent flows. Annu. Rev. Fluid Mech. 32, 203–240.
Weatherly, G.L., Martin, P.J., 1978. On the structure and dynamics of the oceanic bottom boundary layer. J. Phys. Oceanogr. 8, 557–570.
Weinstock, J., 1978. On the theory of turbulence in the buoyancy subrange of stably stratified flows. J. Atmos. Sci. 35, 634–649.
Winters, K.B., 2015. Tidally driven mixing and dissipation in the boundary layer above steep submarine topography. Geophys. Res. Lett. 42, 7123–7130. https://doi.org/10.1002/2015GL064676.
Wunsch, C., 1970. On oceanic boundary mixing. Deep-Sea Res. 17, 293–301.
Wynne-Cattanach, B.L., et al., 2024. Observational evidence of diapycnal up-welling within a sloping submarine canyon. Submitted.